Piezoelectric Nanotopography Induced Neuron-Like Differentiation of Stem Cells

Xiaodi Zhang, Xin Cui, Diancan Wang, Shu Wang, Zhirong Liu, Gengrui Zhao, Yan Zhang, Zhou Li,* Zhong Lin Wang,* and Linlin Li*

The biophysical characteristics of the extracellular matrix, such as nanotopography and bioelectricity, have a profound influence on cell proliferation, adhesion, differentiation, etc. Recognition of the function of a certain biophysical cue and fabrication of biomaterial scaffolds with specific properties would have important implications and significant applications in tissue engineering. Herein, nanotopographic and piezoelectric biomaterials are fabricated and the combination effect of and individual contribution to proliferation, adhesion, and neuron-like differentiation of rat bone marrow-derived mesenchymal stem cells (rbMSCs) are clarified via nanotopography and piezoelectricity. Piezoelectric polyvinylidene fluoride with nanostripe array structures is fabricated, which can generate a surface piezoelectric potential up to millivolt by cell movement and traction. The results reveal a more favorable effect on neuron-like differentiation of rbMSCs from the combination of piezoelectricity and nanotopography rather than nanotopography alone, whereas nanotopography can increase cellular adhesion. This research provides a new insight into designing biomaterials for the potential application in neural tissue engineering.

1. Introduction

Neural regeneration armed at repairing central nervous system, including brain and spinal cord injury, poses great challenges in clinic.[1] To achieve this goal, acquiring sufficient quantity of neuron cells is demanding and challenging due to their weak capability to proliferate. To overcome this obstacle, directed differentiation of stem cells into neurons has been developed for cell replacement therapy.[2–5] In natural stem cell niche,

the biophysical properties of extracellular matrix, e.g., nanotopography,[6–10] stiffness,[11–14] and bioelectricity,[15–18] have sophisticated influence on the behavior of stem cells, including their adhesion, self-renewal, migration, and differentiation.[19,20] The mechanisms of such influence on cells often differ from those of biomolecules and chemicals. Recent efforts have focused on identifying the distinctive function of each biophysical cue and fabricate biomaterial scaffolds to mimic the favorable ones.[21] For instance, it has been found that surface nanotopography of biomaterial scaffolds could direct cytoskeletal organization and focal adhesion (FA) formation, which in turn activate downstream cell signaling and regulate cell behavior via cell mechanotransduction pathway.[22,23] Moreover, some researchers have found that aligned nanogeometry is able to guide neural alignment and polarity, and even provides assistance for neural differentiation of stem cells.[24–27] Nevertheless, aligned nanogeometry alone is still inefficient and suboptimal for directly directing the differentiation of stem cells.

Bioelectricity as a kind of biophysical cue is a crucial guidance for cell proliferation/differentiation, embryonic development, and tissue regeneration. With this foundation, researchers have prepared conductive scaffolds, sometimes along with electrical stimulation, to enhance the neural differentiation of stem cells.[17,18,28] Nonetheless, most electrical

X. D. Zhang, X. Cui, Dr. S. Wang, Z. R. Liu, Dr. G. R. Zhao, Prof. Y. Zhang, Prof. Z. Li, Prof. Z. L. Wang, Prof. L. L. Li
CAS Center for Excellence in Nanoscience
Beijing Institute of Nanoenergy and Nanosystems
Chinese Academy of Sciences
Beijing 100083, P. R. China
E-mail: zli@binn.cas.cn; zhong.wang@mse.gatech.edu; lilinlin@binn.cas.cn

X. D. Zhang, X. Cui, Dr. S. Wang, Z. R. Liu, Dr. G. R. Zhao, Prof. Y. Zhang, Prof. Z. Li, Prof. Z. L. Wang, Prof. L. L. Li
School of Nanoscience and Technology
University of Chinese Academy of Sciences
Beijing 100049, P. R. China

The ORCID identification number(s) for the author(s) of this article can be found under https://doi.org/10.1002/adfm.201900372.

DOI: 10.1002/adfm.201900372

X. Cui, Prof. Y. Zhang, Prof. Z. Li, Prof. Z. L. Wang, Prof. L. L. Li
Center on Nanoenergy Research
School of Physical Science and Technology
Guangxi University
Nanning 530004, P. R. China

Dr. D. C. Wang
Department of Oral and Maxillofacial Surgery
Peking University School and Hospital of Stomatology
Beijing 100081, P. R. China

Prof. Y. Zhang
School of Physics
University of Electronic Science and Technology of China
Chengdu 610054, P. R. China

Prof. Z. L. Wang
School of Materials Science and Engineering
Georgia Institute of Technology
Atlanta, GA 30332-0245, USA

**ADVANCED
SCIENCE NEWS**

www.advancedsciencenews.com

**ADVANCED
FUNCTIONAL
MATERIALS**

www.afm-journal.de

stimulation devices require an external energy input and wire connection, which may increase the risk after implantation. To realize self-powered electrical stimulation, more recently, our and another group have fabricated self-powered triboelectric nanogenerator to stimulate the differentiation of primary mouse embryonic fibroblasts[15] and mesenchymal stem cells[16] into neuron lines. Nevertheless, it still requires wire to connect implanted electrodes for cell stimulation. Accordingly, scaffolds that could realize electrode-less and battery-free electrical stimulation would be promising for tissue regeneration.

Inside human bodies, many biomacromolecules of high-order structures and low-symmetry inherent polarization exhibit piezoelectricity, such as collagen[29] and deoxyribonucleic acids (DNA).[30,31] This property plays important roles in tissue growth and remodeling by intersecting electrical, mechanical, and chemical activities. Bionically, piezoelectric scaffolds have been proven to be able to affect cell behavior through their piezoelectric potential generated from internal or external mechanical force. Several studies have synthesized piezoelectric nanoceramics to improve bone regeneration[32,33] and neuronal stimulation.[34] Despite these progresses, it remains challenging to fabricate piezoelectric scaffolds that could mimic cell microenvironment and guide stem cell differentiation by internal force induced piezoelectricity.

Herein, we hypothesize that piezoelectric and nanotopographic biointerfaces could substantially influence the fate of stem cells. We fabricated two piezoelectric polyvinylidene fluoride (PVDF) nanostripe array structures (ridge, groove, and height were all 200 or 500 nm, respectively) to significantly maximize the generated piezoelectric potential by cell adhesion and migration. We comprehensively investigated the respective effect of piezoelectricity and nanotopography on cell proliferation, focal adhesion formation, and neuron-like differentiation of rat bone marrow-derived mesenchymal stem cells (rbMSCs). Our results revealed a more favorable effect on neuron-like differentiation in both cell morphology and gene/protein expression from the combination of piezoelectricity and nanotopography, compared with nanotopography alone. This finding of the piezoelectric and nanotopographic biomaterials may provide new insight for rational design of scaffolds for neural tissue engineering.

2. Results and Discussion

2.1. Fabrication of Piezoelectric PVDF with Nanoscaled Stripe Arrays

Previous studies have confirmed that stripe arrays with ridge/groove in the range of 200 to 1000 nm can provide assistance for the neural differentiation of stem cells.[8,26,35] To clarify the structure effect of the stripe assays, two kinds of PVDF films with distinct stripe arrays and identically structured polyvinyl chloride (PVC) films are replicated from homostructural silicon molds: one with a repetition period of 400 nm (ridge, groove, and height were all 200 nm, denoted as PVDF-200), whereas the other has a repetition period of 1000 nm (ridge, groove, and height were all 500 nm, denoted as PVDF-500).

Procedures of fabricating silicon molds with different nanoscaled stripes (repetition period of 400 and 1000 nm for

Si-200 and Si-500, respectively) and the duplicated piezoelectric PVDF and nonpiezoelectric PVC nanostructures are shown in **Figure 1**a. Briefly, a silicon wafer coated with positive electron beam resist was exposed to electron beam and transferred onto the crystalline silicon by an inductively coupled plasma (ICP). The residual resist was then removed to yield the final silicon molds. After thorough cleaning of the silicon molds, the PVDF or PVC solution was dropwise added onto the surfaces. After solidification, the PVDF were peeled and followed by thermal annealing to increase the piezoelectric β-phase crystallinity.[36] All the silicon molds can be reused for the fabrication of polymer nanostructures, making the whole process cost-effective and replicable.

Top-view scanning electron microscopy (SEM) images of silicon molds indicated a highly uniform width of ridges and grooves, 200 nm (Figure 1b) and 500 nm (Figure 1c), which were also identically preserved in replicated polymer films (Figure 1d,e). Moreover, cross-section imaging of the polymer films from focus-ion-beam scanning electron microscopy (FIB-SEM) (inset, Figure 1d,e) revealed the height of stripes on the PVDF-200 and the PVDF-500, which were ≈200 and 500 nm, respectively. The structure of the PVC-200 and the PVC-500 was similar with corresponding PVDF (Figure S1, Supporting Information).

In the X-ray diffraction (XRD) spectra, both PVDF samples (PVDF-200 and PVDF-500) exhibited obvious diffraction peaks at $2\theta = 18.53°$, corresponding to the (020) reflection of α-phase of PVDF (**Figure 2**a). We also noticed a clear diffraction peak at around 20.35°, representing the (200)/(110) reflection of the β-phase of PVDF. Therefore, α and β phases coexisted in the PVDF samples. The intensity ratio of the β-phase peak (I_β) to the α-phase one (I_α) was 1.91 and 1.77 for the PVDF-200 and the PVDF-500, respectively. The relatively larger I_β/I_α of the PVDF-200 indicated that the smaller width of stripes might be favorable for the ordered arrangement of molecular chains.
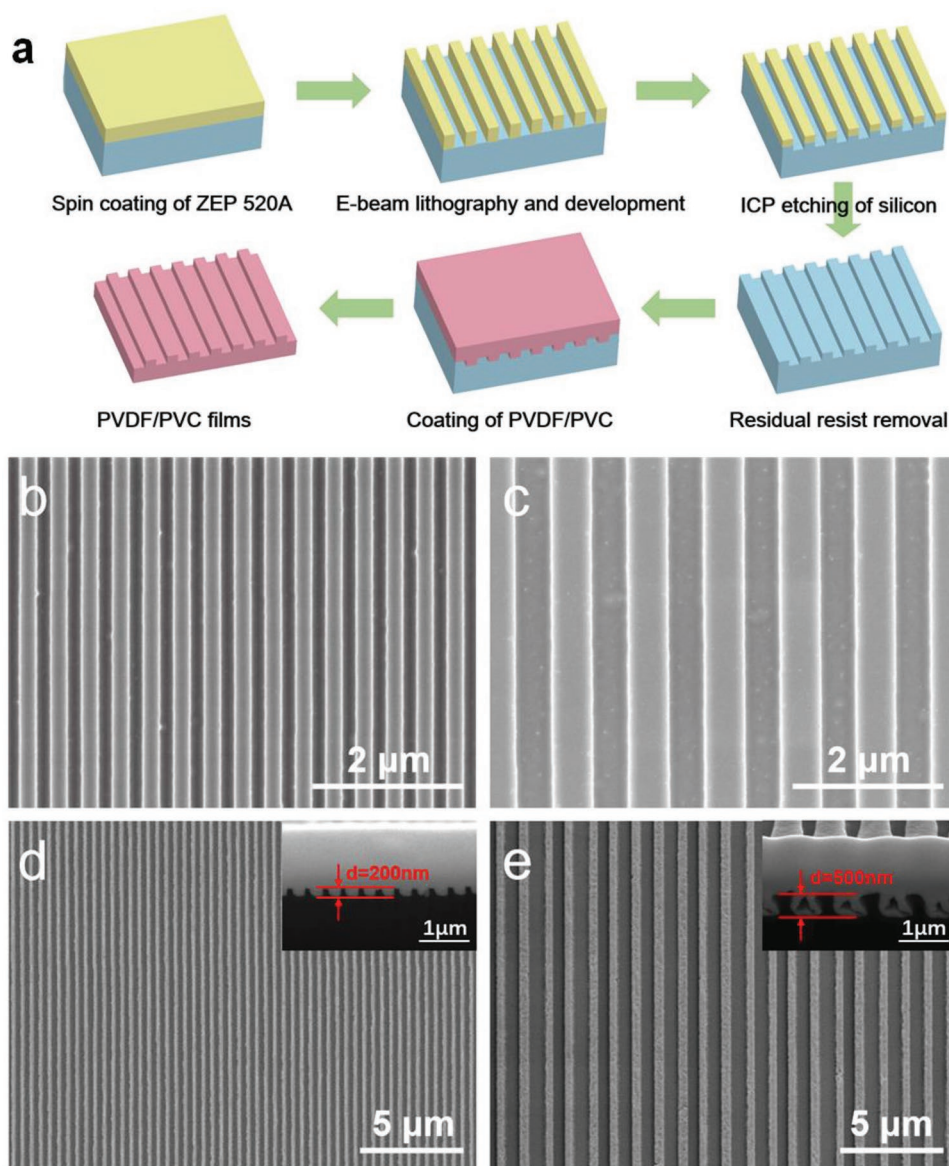
The existence of the piezoelectric β-phase in the PVDF films was further confirmed by Fourier transform infrared (FT-IR) spectroscopy. The characteristic band at 840 cm^{-1} was attributed to the β-phase, whereas the peak at 762 cm^{-1} was designated as the α-phase (Figure 2b).[37] The following equation was used to calculate the β-phase fraction

$$F(\beta) = \frac{A_\beta}{1.26 A_\alpha + A_\beta} \tag{1}$$

where $F(\beta)$ is the fraction of β-phase, A_α is the peak intensity at 762 cm^{-1}, and A_β is the peak intensity at 840 cm^{-1}.[38] $F(\beta)$ of the PVDF-200 (0.54) was higher than that of the PVDF-500 (0.47), in consistent with the XRD data.

We also monitored the electric field (P–E) loop of the PVDF-200 and PVDF-500 (Figure 2c) to determine their remnant polarization (P_r) and saturated polarization (P_s) values. The PVDF-200 and the PVDF-500 had distinct P_r values, 42 and 27 mC m^{-2}, respectively. In addition, the P_s value of the PVDF-200 reached 55.7 mC m^{-2} under 120 MV m^{-1}, whereas the PVDF-500 yielded a P_s value of 42.5 mC m^{-2} under 160 MV m^{-1}. These results also suggested that the PVDF-200 exhibited better piezoelectricity than the PVDF-500.

This argument was further confirmed by piezoresponse force microscopy (PFM). In the measurements, a doped diamond

ADVANCED
SCIENCE NEWS
www.advancedsciencenews.com

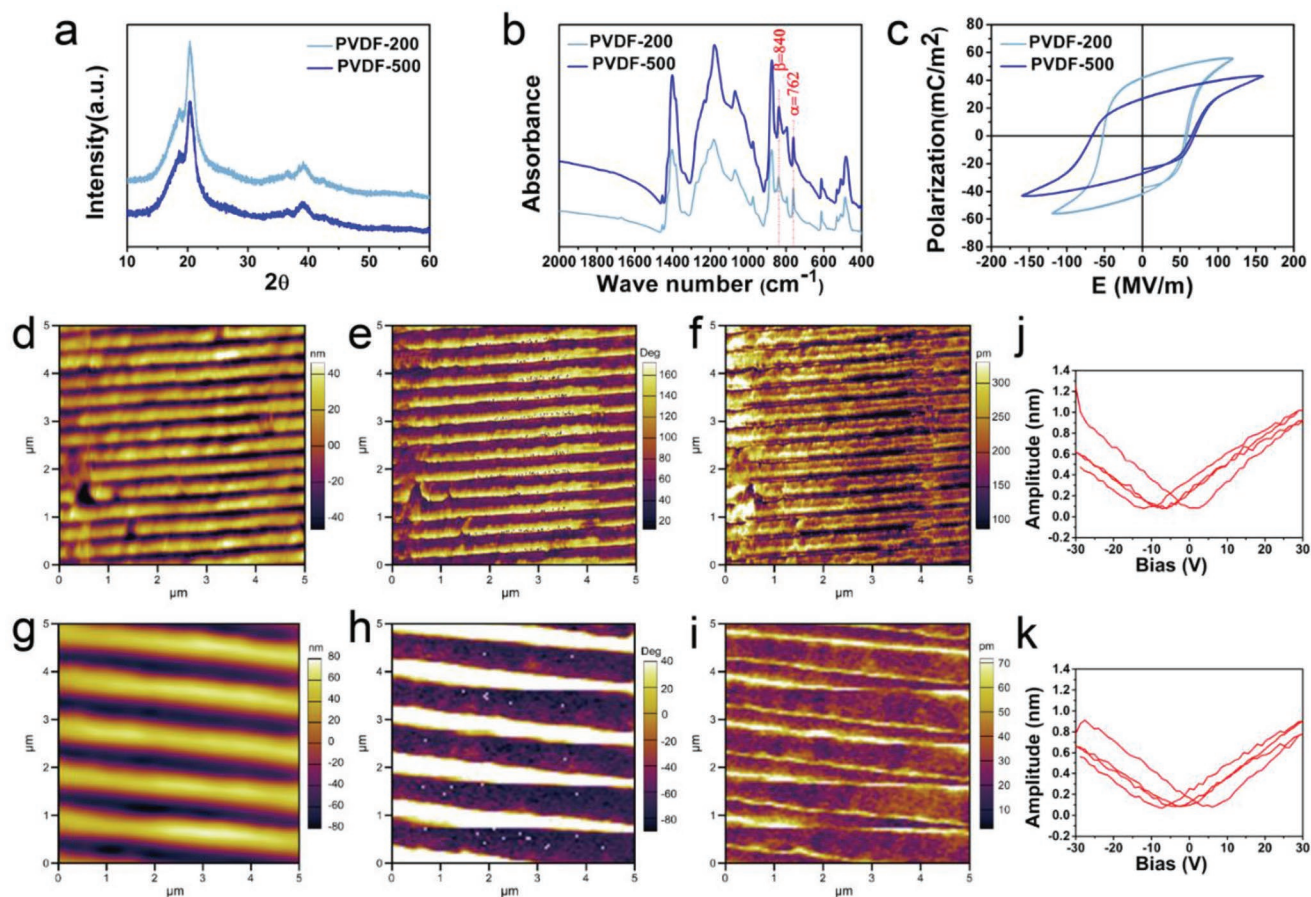ADVANCED
FUNCTIONAL
MATERIALS
www.afm-journal.de

Figure 1. Fabrication and morphology of the PVDF films with different nanoscaled stripes. a) The schematic illustration of fabrication procedure of PVDF/PVC films. SEM images of the silicon molds with repetition period of b) 400 nm (ridge, groove, and height were all 200 nm) and c) 1000 nm (ridge, groove, and height were all 500 nm). SEM images of d) the PVDF-200 (ridge, groove, and height were all 200 nm) and e) the PVDF-500 (ridge, groove, and height were all 500 nm).

PFM tip was used as a top electrode together with a grounded bottom Pt electrode. By scanning an area of 5×5 μm^2, the atomic force microscope (AFM) topography, phase and resolved operational amplifiers (OP) amplitude images of the PVDF films were obtained by PFM. The topographic images (Figure 2d,g) show homogeneous grating structure of the two stripe arrays, in consistent with the SEM data. More importantly, the amplitude of the hysteresis loops, analyzed as a function of applied DC voltage from −30 to +30 V (Figure 2j,k), suggested different piezoelectricity of the two PVDF films. For the PVDF-200, the amplitude reached 1.2 and 0.8 nm under the highest negative and positive bias, respectively. By contrast, the PVDF-500 yielded an amplitude of 0.9 and 0.8 nm under the highest negative and positive bias, respectively. The higher amplitude

of hysteresis loops of the PVDF-200 revealed its higher piezoelectricity than that of PVDF-500. Phase hysteresis loops of the PVDF-200 and the PVDF-500 were shown in Figure S2 in the Supporting Information. Furthermore, the hysteresis loops of phase and amplitude of the PVC films indicated no piezoelectricity (Figure S3, Supporting Information).

2.2. Cytocompatibility and Cell Attachment

For studying the potential neural induction of the piezoelectric PVDF films, multipotent rbMSCs were used here with their pluripotency and high plasticity.[39] With the piezoelectric and nanotopographic characteristics, the influence of the polymer

**ADVANCED
SCIENCE NEWS**
www.advancedsciencenews.com
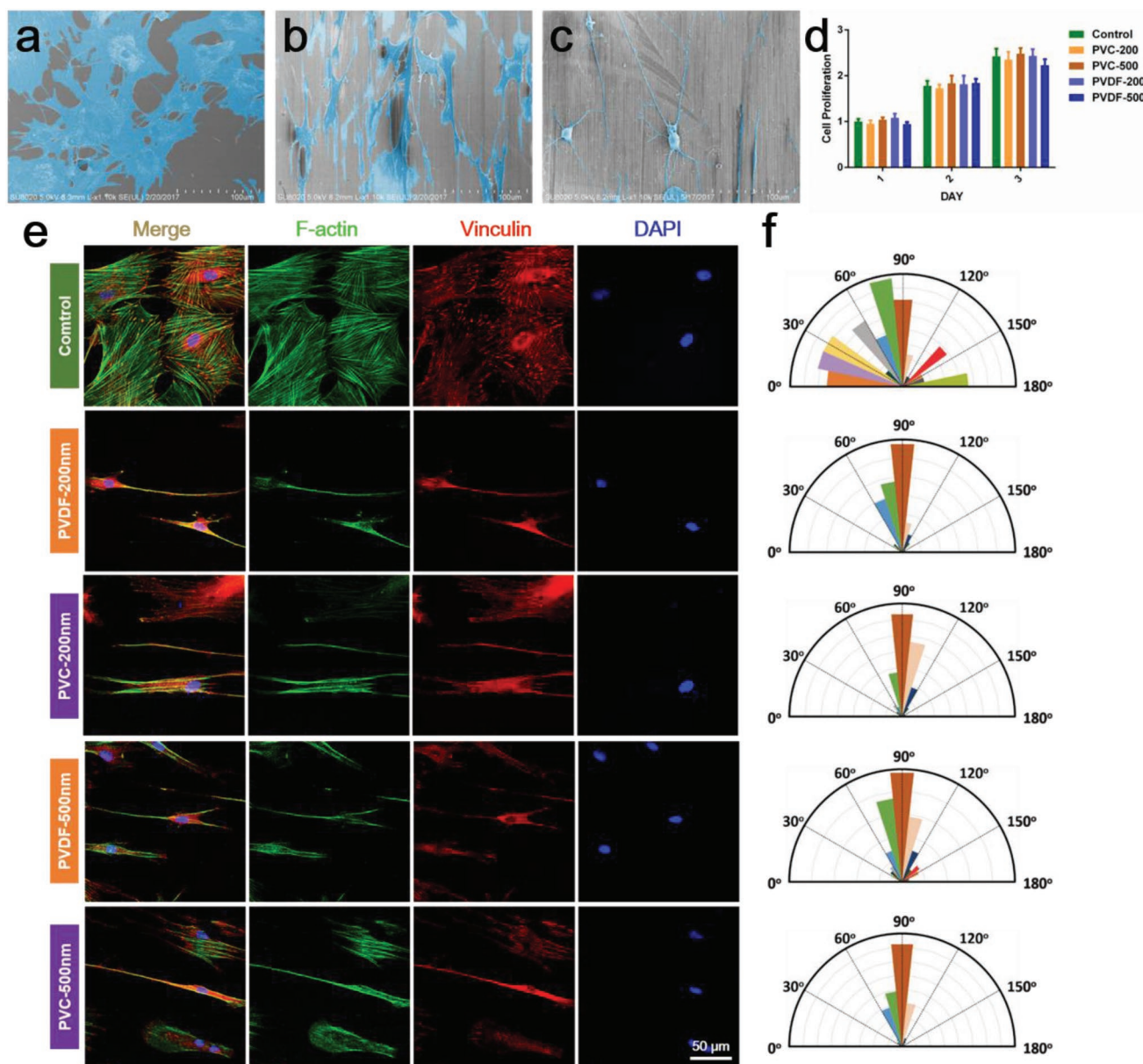
**ADVANCED
FUNCTIONAL
MATERIALS**
www.afm-journal.de

Figure 2. Characterization of crystallization and piezoelectricity of the PVDF films. a) XRD spectra, b) FT-IR spectra, and c) hysteresis loops of the PVDF-200 and the PVDF-500. AFM topography, phase, and resolved OP amplitude images of d–f) the PVDF-200 and g–j) the PVDF-500. Amplitude hysteresis loops of j) the PVDF-200 and k) the PVDF-500.

films on the proliferation and attachment of rbMSCs was discussed. In order to improve the hydrophilicity of the films for enhancing cell adhesion on them, the films were treated with oxygen plasma before cells were seeded on them. The water contact angle (CA) of different samples before and after plasma treatment was showed in Figure S4 in the Supporting Information. The results showed that the existence of nanostripes and oxygen plasma treatment can effectively improve the hydrophilicity of the films. Compared with flat PVDF (water CA = 113.8°), nanostriped PVDF-200 and PVDF-500 without plasma treatment had increased hydrophilicity with CA of 82.9° and 84.6°, respectively. Plasma treatment further decreased CA of PVDF-200 and PVDF-500 to 64.3° and 66.2°, respectively. Specifically, we compared cellular morphology and proliferation of the rbMSCs cultured 3 d on the surface of three different interfaces, PVDF with both piezoelectricity and nanotopography, PVC with only nanotopography, and flat tissue culture plate (TCP). In the result, the cells grew along the stripe array on the surface of PVDF-200, PVDF-500, PVC-200, and PVC-500, whereas they randomly orientated on the flat TCP (**Figure 3**a–c). In addition, the cells on the PVDF developed longer filopodia and more protrusions compared with those on the TCP, yielding tighter attachment to the substrate surface.

From cell proliferation cell count kit-8 (CCK-8 assay), we found similar proliferation rate of the rbMSCs on all the substrates of PVDF, PVC and TCP, within the first two days of culture (Figure 3d). It suggested that both the PVDF and the PVC were biocompatible. On the 3rd day, cell quantities on the PVDF were slightly lower than those on the other two surfaces. No significant difference was observed between the PVDF with different stripe widths as well as that on the PVC.

Furthermore, the cell adhesion was evaluated by fluorescent staining of F-actin and vinculin to visualize cytoskeleton and the FAs distribution. The cells on both the PVDF and the PVC developed alignment along the stripe array, in consistent with that observed from SEM images (Figure 3e and Figure S5, Supporting Information). In particular, both the nuclei angle (Figure 3f) and the cytoskeleton (F-actin) (Figure S6, Supporting Information) inside these aligned cells exhibited obvious orientation. It had a narrow angle distribution of cell nuclei on the aligned stripe array and a broad distribution on the TCPs. On the TCPs, cell nuclei were randomly oriented, which had a standard deviation of cell nuclear angle distribution of 69.47° ± 8.73°. In contrast, cell nuclei were aligned along the direction of stripe direction and the standard deviation of cell nuclear angle distribution on PVDF-200, PVC-200, PVDF-500, and PVC-500 were 23.99° ± 1.34°, 19.68° ± 1.87°, 22.90° ± 2.06°, and 21.37° ± 2.31°, respectively.

ADVANCED
SCIENCE NEWS
www.advancedsciencenews.com

ADVANCED
FUNCTIONAL
MATERIALS
www.afm-journal.de

Figure 3. Cytocompatibility and cell attachment. Representative SEM images of cell spreading of the rbMSCs cultured for 3 d on a) the TCPs, b) the PVDF-200, and c) the PVDF-500. d) Histogram of the statistical results of the cell proliferation rate. All the values were normalized against that grown for 1 d of the control group. e) Immunostaining of focal adhesion protein vinculin. The images are merged images of DAPI (blue fluorescence), F-actin (green fluorescence), and vinculin (red fluorescence). f) Corresponding angular histograms of cell nuclear angles from results in (e).

When growing on the TCPs, the cells mainly expressed vinculin in their perinuclear and pericellular region. The cells on PVDF and PVC, however, more evenly expressed vinculin in the center and at the periphery. More importantly, compared with that on the TCP, the vinculin expression was significantly enhanced on both the PVDF (3.2–3.3-fold enhancement) and the PVC (2.8–3-fold enhancement) (Figure S7, Supporting Information). Meanwhile, there were no significant statistical differences of vinculin expression between the cells on the PVDF and the PVC, and those with different nanoscaled stripes. These results suggested that the nanoscaled stripe arrays with different material properties had similar influence on the adhesion and proliferation of rbMSCs. In addition, from the protein adsorption results (Figure S8, Supporting Information), bovine serum albumin (BSA) had about 9–10.5-fold protein adsorption qualities on nanostriped PVDF and PVC surfaces, compared with that on flat PVDF. The adsorption protein had no obvious differences among the nanostriped samples. So we could exclude the difference in protein absorption on differentiation. Thus, we could conveniently distinguish whether the piezoelectricity or the surface morphology has a greater effect on cell differentiation as the effect of morphology is the same.

2.3. Neuron-Like Differentiation of rbMSCs

To determine whether the piezoelectric and nanotopographic interfaces could mediate spontaneous neuron-like differentiation of rbMSCs, the fetal bovine serum (FBS) concentration in the cell culture medium was reduced from 10% to 1% to terminate the cell proliferation after their adhesion to substrates. After 7 d culture, the cells were immunofluorescently stained with a neuron specific maker, β-Tubulin III (Tuj-1), and a neurogliocyte specific maker, glial fibrillary acidic protein (GFAP) (**Figure 4**).

We found significantly more Tuj-1 positive cells on the PVDF-200 and the PVDF-500 interfaces compared with those
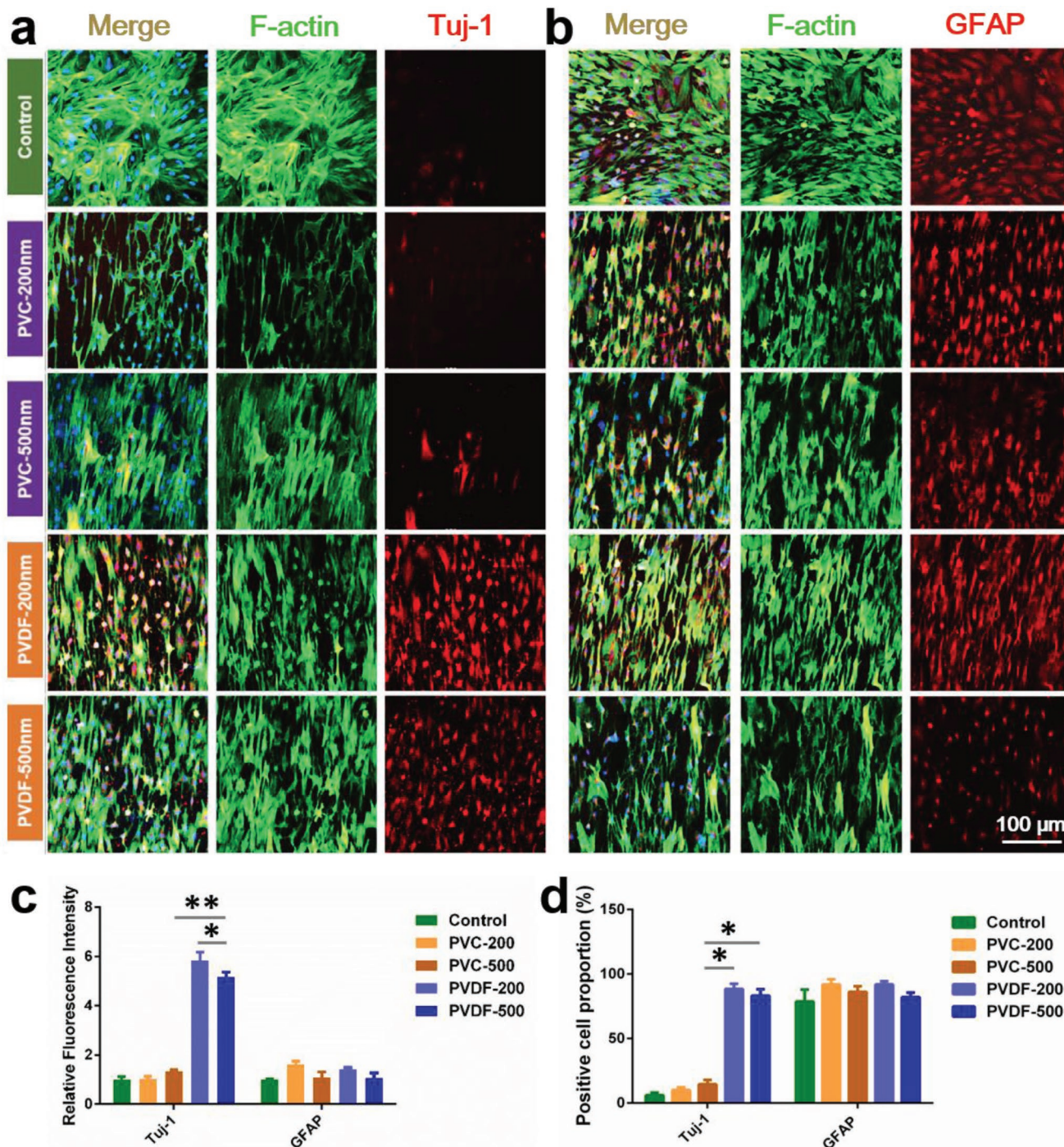
Figure 4. a) Immunofluorescent staining of the neuron specific maker Tuj-1 and b) a neurogliocyte specific maker GFAP after 7 d culture. The cell nuclei were stained with DAPI (blue) and F-actin was stained with phalloidin-Alexa Fluor 488 (green). Tuj-1 and GFAP were immunostained, respectively (red). c) Statistical analysis of the fluorescence intensity of Tuj-1 and GFAP with Image-Pro Plus 6.0. d) Statistical analysis of the percentage of Tuj-1 positive cells and GFAP positive cells.

on the TCPs and the PVC (PVC-200 and PVC-500) (Figure 4a), while the quantity of GFAP-positive cells was similar on the TCPs, the PVDF, and the PVC (Figure 4b). Quantitative analysis of the fluorescent intensity indicated 5.85 and 5.16-fold more Tuj-1 positive cells on the PVDF-200 and PVDF-500 than on the flat control surface, respectively (Figure 4c). In contrast, the corresponding values were 1.04 and 1.35-fold for the PVC-200 and the PVC-500, respectively (Figure 4c). In addition, the percentage of Tuj-1 positive cells were 14.4, 8.64, 6.05, and 1.06-fold on the PVDF-200, the PVDF-500, the PVC-200, and the PVC-500, respectively, compared with that on the flat control surface (Figure 4d). Interestingly, cells grown on flat PVDF had no expression of Tuj-1 (Figure S9, Supporting Information).

Importantly, our results suggested a positive effect of piezoelectricity on the neuron-like differentiation of rbMSCs. First, different from the spindle and flat cellular morphology on TCPs and the PVC, the cells on the PVDF-200 and the PVDF-500 developed a neuron-like morphology, including highly refractile cell bodies and thin elongated pseudopods that terminated in structures resembling growth cones. Moreover, the quantity of the Tuj-1 positive cells was higher on the PVDF-200 surface than that on the PVDF-500. These results suggested that the piezoelectricity rather than the nanotopography of stripe array nanostructure could enhance neuron-like differentiation of the rbMSC.

To further detect the neuron-like differentiation at the gene level, a quantitative reverse transcription polymerase chain reaction (RT-qPCR) assay was used to analyze the mRNA levels of typical markers of neural cells, i.e., Tuj-1, GFAP, and microtubule-associated protein-2 (MAP-2), after 7 d of rbMSC neurogenesis (**Figure 5**a–c). Compared with the cells on the TCP, the level of cellular Tuj-1 mRNA on the PVDF-200, the PVDF-500, the PVC-200 and the PVC-500 increased 1.70, 1.53, 1.19, and 1.26-fold, respectively. The level of MAP-2 mRNA of the cells on the PVDF-200, PVDF-500, PVC-200, and PVC-500 were 1.50, 1.48, 1.36, and 1.24-fold of that on the TCP, respectively. While the GFAP expression on the PVC and the PVDF surfaces was close to each other, both of them were higher than that on the TCP. These results revealed the piezoelectric biointerface with nanotopography could provide important biophysical cues to induce neuron-like differentiation of stem cells.

In this work, we propose that the traction force of living cells on the nanostriped PVDF surface could induce the deformation of PVDF stripe, thus creating a local piezoelectric potential. The local piezoelectric potential near the cell membrane would provide continuous electric stimulation for the living cells as long as the cells are under movement.[40] Typically, the cell traction force is in the nN range (0.1–10 nN).[41,42] We simulated the piezoelectric potential generated from cell motion on the piezoelectric nanotopography by COMSOL Multiphysics (**Figure 6**). As a boundary condition, the bottom of the PVDF film was fixed and grounded. A force of 0.1–10 nN was applied along the γ-axis at the top of the strip. As a result, the PVDF-200 generates piezoelectric potential from 34 µV to 3.4 mV, and PVDF-500 generated piezoelectric potential from 29.4 µV to 2.94 mV with cell traction forces increased from 0.1 to 10 nN (Figure 6b,c and Figure S10, Supporting Information). The results showed that the PVDF-200 generated a slightly higher piezoelectric potential than the PVDF-500 when identical cell traction force was applied. In contrast, when the cell traction force was also 10 nN, the piezoelectric potential generated by cell traction force on flat PVDF film without nanoscaled stripe array was only 960 nV, which was insignificant for the physiological activity of the cell (Figure S11, Supporting Information). In other words, nanotopography of the PVDF film could increase the generated piezoelectric potential in response to cell migration and traction, providing a stronger signal to stimulate the differentiation of stem cells.

3. Discussions

Both piezoelectricity and nanotopography are considered as important biophysical cues to determine the stem cell fate, yet their effects are often interpreted separately. By fabricating nanopatterned piezoelectric biointerfaces, herein, we first clarified how these two biophysical cues together could direct neural differentiation of stem cells more efficiently. By fabricating piezoelectric PVDF with two kinds of nanostripe array structures and using identical nonpiezoelectric PVC nanostructures as the controls, we identified a more significant contribution from piezoelectricity than nanotopography.

Recently, studies have found that human neural stem cells (hNSCs) had significantly increased expression of focal adhesion kinase (FAK) and vinculin when growing on substrates with aligned morphology.[23] Such nanopatterned substrates facilitate the focal adhesion formation and FAK phosphorylation, thus activating the mitogen-activated protein kinase-extracellular regulated protein kinases (MEK-ERK) signaling pathway to promote neural differentiation of hNSCs into
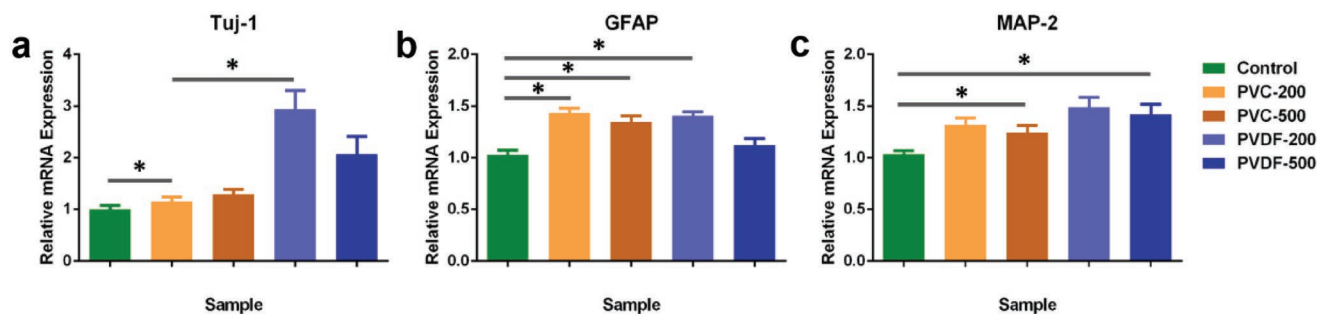
Figure 5. Relative mRNA expression of a) Tuj-1, b) GFAP, and c) MAP-2 after rbMSC neurogenesis for 7 d. The values were normalized against GAPDH level of control cells on day 7 and the gene expression level of cells on TCP is considered as "1" ($* p < 0.05$).
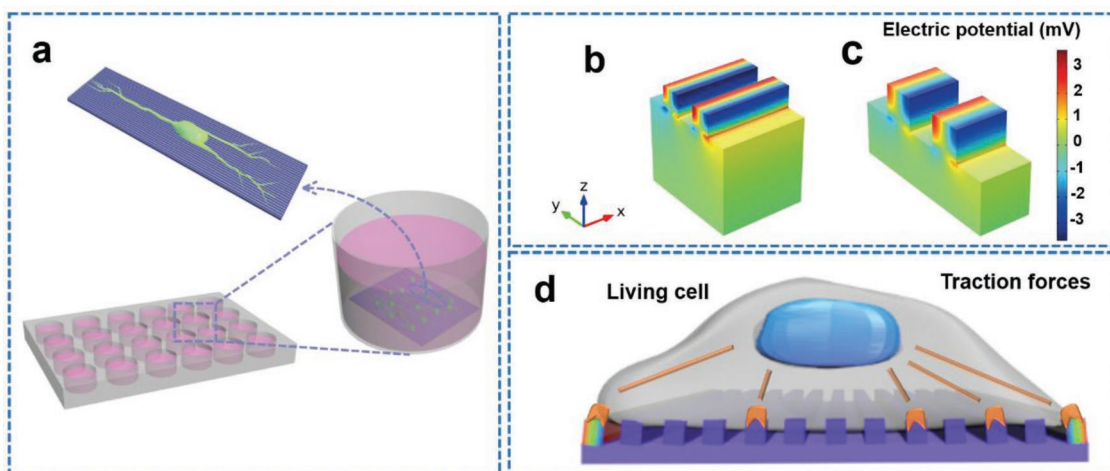
Figure 6. a) Schematic diagram of the MSC neuron-like differentiation on the PVDF substrate. COMSOL simulation of b) the PVDF-200 generating a maximum positive voltage of 3.4 mV when strained by a tangential force of 10 nN, where Fs 2.93 mV was generated by c) the PVDF-500. d) Inherent cell forces of living cells grown on the surface of PVDF with nanoscaled stripe arrays.

neurons or astrocytes. Our results were in consistent with these findings, where cells on the PVC and the PVDF with nanostripe arrays showed increased expression of vinculin and GFAP compared with that on the flat TCP (Figure 3).

Piezoelectric potential has been proven to provide electrical stimulation to the cells, which is beneficial for cell proliferation, attachment, differentiation and synaptic extension.[43] On the other hand, physiological activities of cells, such as adhesion and migration, can induce the generation of piezoelectric potential by generating minute deformation of the substrate ridges.[44] It is speculated that the local electric field produced near the cell plasma membrane could tune cell activity and signaling, and finally induce the differentiation of cells.[40]

Our subsequent experiments of cell differentiation proved the hypothesis. The expressions of Tuj-1, GFAP, and MAP-2 of cells on the PVC and the PVDF increased by different degree depending on the piezoelectricity rather than the nanotopography of the substrates (Figure 4). Additionally, there were more Tuj-1 positive cells on the PVDF-200, which had a higher crystallinity and piezoelectricity than the PVDF-500, excluding the influence of nanotopography. All the results suggested that piezoelectricity had a more positive effect on neuron-like differentiation compared with nanotopography. It was worth noting that cells on the PVC films had an increased GFAP expression more significantly than Tuj-1 and MAP-2, whereas the PVDF substrates preferably directed the differentiation into Tuj-1+ cells with neuron-like morphology, possibly stimulated by the piezoelectricity of the substrates. Hence, our piezoelectric biointerfaces with nanoscaled stripe arrays allow sensitive structure deformation in response to the cellular activities and the elongation of filopodia, thereby generating more significant piezoelectric potential to stimulate neuron-like differentiation of stem cells. It should be noted that in spite of that the neural phenotypes (neural like morphology and gene expression) have been observed from the induction of piezoelectric nanotopography, the underling mechanism of the transdifferentiation should be further studied, and the function of induced neuron-like cells should be researched.

4. Conclusion

In summary, this study demonstrated that the piezoelectric PVDF with nanoscaled stripe array, which could generate surface piezoelectric potential by cell traction, manipulated the neuron-like differentiation of the rbMSCs. The rbMSCs on the PVDF stripe array differentiated into β-III tubulin+ neuron-like cells, which was not happened for those on the nonpiezoelectric PVC stripe array, proving that piezoelectricity tended to guide the rbMSCs to differentiate into neurons. Our research provides new insight and approach for the application of piezoelectric materials in neural tissue engineering.

5. Experimental Section

Fabrication of the Nanoscaled Stripe Arrays: The silicon mode with nanoscaled stripe structure was fabricated from a clean silicon wafer. The wafer was coated with a positive electron beam resist (ZEP-520A) with a 300 nm thickness and exposed using electron beam lithography (Vistec EBPG 5000+). Then it was transferred onto the crystalline silicon by subsequent etching using an ICP (Plasmalab System 100 ICP 180) etcher with a mixture of SF_6 and CHF_3. Finally, the residual resist was removed at room temperature (RT) using the resist remover.

For the polymeric nanostructure, PVDF (number-average molecular weight of 5.34×10^5 Da, Aldrich) or PVC (7.2×10^4 Da, Aldrich) was dissolved in *N*-dimethylformamide with a concentration of 6% w/v. The solution was casted onto the silicon templates. After being dried at 60 °C in an oven for 10 h to completely evaporate the residual solvent, the PVDF (or PVC) films with nanoscaled stripe array were carefully peered off from the silicon mold in an aqueous solution. Then, the films were annealed in an oven at 135 °C for 6 h to increase the crystallinity. The total film had a thickness of about 30 μm. In the following experiments, PVDF films with 200 and 500 nm stripe (both width and depth) were labeled as PVDF-200 and PVDF-500, and PVC films with 200 and 500 nm stripes were labeled as PVC-200 and PVC-500, respectively. Each side the films were treated with oxygen plasma using Plasma Cleaning System (PVA TePla/IoN 40, America) for 3 min to improve hydrophilicity and cell attachment.

Characterization: The nanostructured films with nanoscaled stripe array were sputter coated with a layer of Au for the observation by SEM (SU8020, Hitachi, Japan) and electron beam focusing ion beam double beam electron microscope (FIB-SEM, FEI, Helios NanoLab

600i, Czech). XRD patterns were measured by a PANalytical X'pert3 diffractometer (PANalytical Ltd., Netherland) from 10° to 60°. FT-IR spectra were performed on Vertex80V (Bruker Corp., USA) in the range of 400–2000 cm^{-1}. Electric field (P–E) loops were tested by a Precision Premier II Ferroelectric Tester (Radiant Technologies Inc., New Mexico, USA). The piezoelectricity of the PVDF films was characterized by PFM (MFP-3D, Asylum Research). Water contact angle was tested by the contact angle measurement (XG-CAMB1, XUANYI).

Protein Absorption Test: To assess the protein absorption ability of the films, they were cut into slices with the same dimension (8 mm × 8 mm). The films were soaked in 1% w/v BSA, followed by incubating under 37 °C for 3 d. Then the films were washed with phosphate buffer saline (PBS) for three times to remove residual proteins. The bicinchoninic acid protein kit was used to quantify protein absorption on these films with standard protocol (samples = 3).

rbMSCs Isolation and Culture: The animals were purchased from Vital River Company (Beijing). All the procedures in handing the animals strictly followed the national standards "Laboratory Animal Requirements of Environment and Housing Facilities (GB14925-2001)." rbMSCs were obtained from femurs and tibias of 4-week-old male Wistar rats. The purified cells were cultured in lowglucose (1.0 g L^{-1}) Dulbecco's modified Eagle medium (Gibco) supplemented with 10% FBS (Gibco) in a humidified atmosphere of 5% CO$_2$ at 37 °C. rbMSCs at the one to three passages were used for the following experiments.

Cell Attachment and Proliferation: All the films with nanoscaled stripe array placed in the 24-well-plates were sterilized by soaking in 75% ethanol for 2 h and exposed to the ultraviolet light for 1 h. After the samples were immersed in the culture medium for 4 h, rbMSCs were seeded on the films at a density of 5.6 × 10^4 cells cm^{-2}. TCPs were used as a flat control. The CCK-8 (Dojindo Molecular Technology) assay was used to quantitatively evaluate the cell proliferation on the samples (n = 5 for each group) after culture for 1, 2, and 3 d, respectively, according to the manufacturer's instructions.

To observe the morphology and attachment of rbMSCs on the stripe array films, rbMSCs seeded on samples were immunfluorescently stained with phalloidin and vinculin antibody to show the filamentous actins (F-actin) and FA distribution. After 48 h incubation on the films, the cells were rinsed with PBS, fixed with 4% formaldehyde for 10 min, permeabilized with 0.1% Triton X-100 for 10 min and blocked with 10% goat serum solution for 1 h at RT. Then, the cells were incubated with the primary vinculin antibodies (rabbit polyclonal, Abcam) overnight at 4 °C. Cy3 labeled goat antirabbit secondary antibody in goat serum solution was incubated for 4 h at RT. To label F-actin, the cells were stained with phalloidin-Alexa Fluor 488 (Invitrogen) for 4 h at RT. After each step, the samples were washed with PBS for three times. Subsequently, 4′,6-diamidino-2-phenylindole (DAPI) at a concentration of 1 μg mL^{-1} was used to stain the cell nuclei for 10 min at RT. The fluorescently stained rbMSCs were observed under a confocal laser scanning microscope (Leica/TCS SP8).

The morphology of cells on the nanoscaled stripe array and TCPs were observed by SEM. rbMSCs cultured on different samples were fixed with 2.5% glutaraldehyde for 2 h. A graded ethanol series (30%, 50%, 70%, 80%, 90%, 95%, 98%, and 100%) were used to dehydrate the cells in sequence. The dried samples were sputter coated with Au and observed with a HITACHI S-8020 scanning electron microscopy.

Differentiation of rbMSCs: rbMSCs (8 × 10^3 cells) were seeded onto different substrates for 4 h (n = 3). rbMSCs were maintained in the complete medium without supplementation of any neurotrophic factors. After 2 d culture, FBS was reduced from 10% to 1% to trigger the spontaneous differentiation induced by piezoelectricity and nanotopography. The differentiation process was lasted for 7 d, and then the cells were analyzed by immunofluorescent staining and RT-qPCR.

Immunofluorescent Staining: Immunofluorescent staining for rbMSCs was performed as previously described.[45] In brief, after differentiation for 7 d, rbMSCs were washed with PBS for three times, fixed with 4% paraformaldehyde for 10 min, and permeabilized with 0.1% Triton X-100 for 10 min. After being blocked with 10% goat serum for 1 h, the cells were incubated with the primary antibodies overnight at 4 °C and then incubated with the secondary antibodies for 4 h at RT. To identify the cells directly, the cells were stained with phalloidin-Alexa Fluor 488 (Invitrogen) for 4 h at RT. Finally, DAPI staining was performed before imaging on Confocal microscope. The primary antibodies included rabbit anti-Tuj1 (Abcam) and mouse anti-GFAP (Abcam) antibodies. The corresponding secondary antibodies were Cy3-conjugated goat antirabbit IgG (Jackson ImmunoResearch) and Cy3-conjugated goat antimouse IgG (1:200, Jackson ImmunoResearch).

RT-qPCR: The cells were treated with TRIZOL Regent (Invitrogen). The total RNA concentration, purity, and integrity were examined on a Q-5000 spectrophotometer (Quawell). The RT-qPCR analysis was performed on a 7500 Real Time PCR system (Applied Biosystems) to detect the mRNA level of Tuj1, GFAP and MAP2. GAPDH was used as the housekeeping gene. The primer sequences designed in the RT-qPCR analysis were as follows:

GAPDH (Forward primers (5′-3′), GCCTCGTCTCATAGACAAGATGGT. Reverse primers (5′-3′), GAAGGCAGCCCTGGTAACC).
Tuj1 (Forward primers (5′-3′), TAGACCCCAGCGGCAACTAT. Reverse primers (5′-3′), GTTCCAGGCTCCAGGTCCACC).
GFAP (Forward primers (5′-3′), CGGAGACGTATCACCTCTG. Reverse primers (5′-3′), TGGAGGCGTCATTCGAGACAA.
MAP2 (Forward primers (5′-3′), GCCAGCATCAGAACAAACAG. Reverse primers (5′-3′), AAGGTCTTGGGAGGGAAGAAC.

Relative levels of the target gene were normalized against GAPDH (n = 3 for each group).

Finite Element Modeling of the Piezoelectric Nanoscaled Stripe Arrays: To calculate the piezoelectric potential of a single PVDF stripe induced by a cell tangential force, the finite element simulation was carried out using COMSOL Multiphysics software. The bottom of the stripe was defined as an anchor or fixed constrain and the upper of the stripe was loaded by the cell force.

Statistical Analysis: Statistics were performed using one-way analysis of variance (ANOVA) in GraphPad Instant Software (GraphPad Software). The data were expressed as mean ± S.D. (standard deviation). The statistical significance of the differences was determined by a one-way ANOVA (* means $p < 0.05$, ** means $p < 0.01$, and NS represents no significance).

Supporting Information

Supporting Information is available from the Wiley Online Library or from the author.

Acknowledgements

Conflict of Interest

The authors declare no conflict of interest.

Keywords

[1] P. Assinck, G. J. Duncan, B. J. Hilton, J. R. Plemel, W. Tetzlaff. *Nat. Neurosci.* **2017**, *20*, 637.

[2] B. Zhang, W. Yan, Y. Zhu, W. Yang, W. Le, B. Chen, R. Zhu, L. Cheng, *Adv. Mater.* **2018**, *30*, 1705694.

[3] T. C. Tseng, L. Tao, F. Y. Hsieh, Y. Wei, I. M. Chiu, S. h. Hsu, *Adv. Mater.* **2015**, *27*, 3518.

[4] L. Gong, L. Cao, Z. Shen, L. Gao, S. Shao, C. Zhang, J. Lu, W. Li, *Adv. Mater.* **2018**, *30*, 1705684.

[5] G. Orive, E. Anitua, J. L. Pedraz, D. F. Emerich, *Nat. Rev. Neurosci.* **2009**, *10*, 682.

[6] J. Kim, J. R. Staunton, K. Tanner, *Adv. Mater.* **2016**, *28*, 132.

[7] J. H. Kim, H. W. Kim, K. J. Cha, J. Han, Y. J. Jang, D. S. Kim, J. H. Kim, *ACS Nano* **2016**, *10*, 3342.

[8] Y. Zhang, A. Gordon, W. Qian, W. Chen, *Adv. Healthcare Mater.* **2015**, *4*, 1900.

[9] T. C. Von Erlach, S. Bertazzo, M. A. Wozniak, C. M. Horejs, S. A. Maynard, S. Attwood, B. K. Robinson, H. Autefage, C. Kallepitis, A. del Río Hernández, *Nat. Mater.* **2018**, *17*, 237.

[10] H. Cao, T. Liu, S. Y. Chew, *Adv. Drug Delivery Rev.* **2009**, *61*, 1055.

[11] K. H. Vining, D. J. Mooney, *Nat. Rev. Mol. Cell Biol.* **2017**, *18*, 728.

[12] N. D. Leipzig, M. S. Shoichet, *Biomaterials* **2009**, *30*, 6867.

[13] G. J. Her, H. C. Wu, M. H. Chen, M. Y. Chen, S. C. Chang, T. W. Wang, *Acta Biomater.* **2013**, *9*, 5170.

[14] E. E. Charrier, K. Pogoda, R. G. Wells, P. A. Janmey, *Nat. Commun.* **2018**, *9*, 449.

[15] Y. Jin, J. Seo, J. S. Lee, S. Shin, H. J. Park, S. Min, E. Cheong, T. Lee, S. W. Cho, *Adv. Mater.* **2016**, *28*, 7365.

[16] W. Guo, X. Zhang, X. Yu, S. Wang, J. Qiu, W. Tang, L. Li, H. Liu, Z. L. Wang, *ACS Nano* **2016**, *10*, 5086.

[17] W. Guo, S. Wang, X. Yu, J. Qiu, J. Li, W. Tang, Z. Li, X. Mou, H. Liu, Z. L. Wang, *Nanoscale* **2016**, *8*, 1897.

[18] S. Wang, J. Qiu, W. Guo, X. Yu, J. Nie, J. Zhang, X. Zhang, Z. Liu, X. Mou, L. Li, H. Liu, *Adv. Biosyst.* **2017**, *1*, 1600042.

[19] R. Ayala, C. Zhang, D. Yang, Y. Hwang, A. Aung, S. S. Shroff, F. T. Arce, R. Lal, G. Arya, *Biomaterials* **2011**, *32*, 3700.

[20] J. Lee, A. A. Abdeen, D. Zhang, K. A. Kilian, *Biomaterials* **2013**, *34*, 8140.

[21] S. M. Willerth, S. E. Sakiyama-Elbert, *Adv. Drug Delivery Rev.* **2007**, *59*, 325.

[22] T. Iskratsch, H. Wolfenson, M. P. Sheetz, *Nat. Rev. Mol. Cell Biol.* **2014**, *15*, 825.

[23] K. Yang, K. Jung, E. Ko, J. Kim, K. I. Park, J. Kim, S. W. Cho, *ACS Appl. Mater. Interfaces* **2013**, *5*, 10529.

[24] J. Xie, M. R. MacEwan, X. Li, S. E. Sakiyama-Elbert, Y. Xia, *ACS Nano* **2009**, *3*, 1151.

[25] J. Xie, M. R. MacEwan, S. M. Willerth, X. Li, D. W. Moran, S. E. Sakiyama-Elbert, Y. Xia, *Adv. Funct. Mater.* **2009**, *19*, 2312.

[26] M. R. Lee, K. W. Kwon, H. Jung, H. N. Kim, K. Y. Suh, K. Kim, K. S. Kim, *Biomaterials* **2010**, *31*, 4360.

[27] K. K. Tan, J. Y. Tann, S. R. Sathe, S. H. Goh, D. Ma, E. L. Goh, E. K. Yim, *Biomaterials* **2015**, *43*, 32.

[28] Y. Wei, X. Mo, P. Zhang, Y. Li, J. Liao, Y. Li, J. Zhang, C. Ning, S. Wang, X. Deng, *ACS Nano* **2017**, *11*, 5915.

[29] S. Guerin, T. A. Syed, D. Thompson, *Nanoscale* **2018**, *10*, 9653.

[30] Y. Zhu, S. Zhang, J. Wen, *Ferroelectrics* **1990**, *101*, 129.

[31] E. Fukada, Y. Ando, *J. Polym. Sci., Part A-2: Polym. Phys.* **1972**, *10*, 565.

[32] X. Zhang, C. Zhang, Y. Lin, P. Hu, Y. Shen, K. Wang, S. Meng, Y. Chai, X. Dai, X. Liu, *ACS Nano* **2016**, *10*, 7279.

[33] A. Marino, S. Arai, Y. Hou, E. Sinibaldi, M. Pellegrino, Y. T. Chang, B. Mazzolai, V. Mattoli, M. Suzuki, G. Ciofani, *ACS Nano* **2015**, *9*, 7678.

[34] G. G. Genchi, L. Ceseracciu, A. Marino, M. Labardi, S. Marras, F. Pignatelli, L. Bruschini, V. Mattoli, G. Ciofani, *Adv. Healthcare Mater.* **2016**, *5*, 1808.

[35] K. Yang, S. J. Yu, J. S. Lee, H. R. Lee, G. E. Chang, J. Seo, T. Lee, E. Cheong, S. G. Im, S. W. Cho, *Nanoscale* **2017**, *9*, 18737.

[36] A. Wang, Z. Liu, M. Hu, C. Wang, X. Zhang, B. Shi, Y. Fan, Y. Cui, Z. Li, K. Ren, *Nano Energy* **2018**, *43*, 63.

[37] Z. Xu, M. Baniasadi, S. Moreno, J. Cai, M. Naraghi, M. Minary Jolandan, *Polymer* **2016**, *106*, 62.

[38] D. Dhakras, V. Borkar, S. Ogale, J. Jog, *Nanoscale* **2012**, *4*, 752.

[39] Y. Jiang, B. Jahagirdar, R. Reinhardt, R. Schwartz, C. Keene, X. Ortiz-Gonzalez, M. Reyes, T. Lenvik, T. Lund, M. Blackstad, J. Du, S. Aldrich, A. Lisberg, W. Low, D. Largaespada, C. Verfaillie, *Nature* **2002**, *418*, 41.

[40] G. Murillo, A. Blanquer, C. Vargas-Estevez, L. Barrios, E. Ibáñez, C. Nogués, J. Esteve, *Adv. Mater.* **2017**, *29*, 1605048.

[41] H. Feng, H. Ouyang, M. Peng, Y. Jin, Y. Zhang, Z. Liu, Y. Zou, C. Zhao, Y. Fan, J. Zhai, Z. L. Wang, Z. Li, *Nano Energy* **2018**, *50*, 504.

[42] G. Weder, J. Vörös, M. Giazzon, N. Matthey, H. Heinzelmann, M. Liley, *Biointerphases* **2009**, *4*, 27.

[43] A. H. Rajabi, M. Jaffe, T. L. Arinzeh, *Acta Biomater.* **2015**, *24*, 12.

[44] J. Friedrichs, A. Taubenberger, C. M. Franz, D. J. Muller, *J. Mol. Biol.* **2007**, *372*, 594.

[45] X. Zhang, W. Guo, J. Qiu, S. Wang, X. Yu, L. Li, H. Liu, *J. Alloys Compd.* **2017**, *729*, 816.